CHEMISTRY OF MATERIALS
Cite This: Chem. Mater. XXXX, XXX, XXX−XXX
Article
pubs.acs.org/cm

Rock-Salt-Type $MnCo_2O_3$/C as Efficient Oxygen Reduction Electrocatalysts for Alkaline Fuel Cells

Yao Yang, Rui Zeng, Yin Xiong, Francis J. DiSalvo, and Héctor D. Abruña*

Department of Chemistry and Chemical Biology, Baker Laboratory, Cornell University, Ithaca, New York 14853, United States

Supporting Information

ABSTRACT: The search for nonprecious metal-based electrocatalysts with high activity and long durability for the oxygen reduction reaction (ORR) has been long pursued by the renewable energy material community. Here, we designed a new Mn−Co bimetallic oxide $MnCo_2O_3$/C with the rock-salt-type structure, derived from a spinel-type precursor $MnCo_2O_4$/C under mild reduction using NH_3 at 300 °C. In-depth electron microscopic and spectroscopic investigations suggest that $MnCo_2O_3$/C predominantly has Mn(II) and Co(II) and can be written as $MnO(CoO)_2$/C. Charge transfer between Mn and Co was probed by electron energy-loss near-edge structure (ELNES) analysis. $MnCo_2O_3$/C has a Co-rich core and a thin 1−3 nm Mn shell with a mesoporous morphology. $MnCo_2O_3$/C achieved a high ORR activity with a half-wave potential of 0.86 V in 1 M KOH, which was ascribed to the microstructure and the synergistic effects between Mn and Co, serving as co-active sites for the ORR.

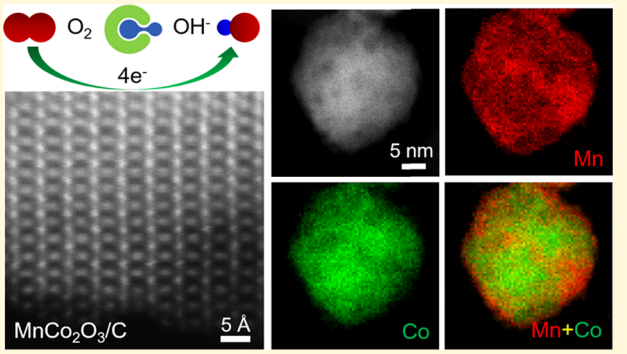

INTRODUCTION

Hydrogen fuel cells have been recognized as one of the key next-generation renewable energy technologies, especially for powering electric vehicles (EVs).[1−4] However, a significant amount of Pt (>0.2 g_{Pt}/kW) is still required to catalyze the sluggish oxygen reduction reaction (ORR) in proton exchange membrane fuel cells (PEMFCs).[5−8] Recently, anion exchange membrane fuel cells (AEMFCs) have emerged as a competitive alternative technology, since they enable the use of nonprecious metals or metal oxides in alkaline media.[9,10] To facilitate the ORR kinetics in alkaline media, the fuel cell community has been devoted to investigating a variety of nonprecious electrocatalysts, including metal-containing nitrogen-doped carbons, perovskites, and transition-metal oxides.[11−18] Metal-containing nitrogen-doped carbons (e.g., Fe−N−C) have shown promising activities in rotating disk electrode (RDE) measurements. However, they generally suffer from poor performance in practical membrane electrode assembly (MEA) tests (peak power density <0.5 W/cm^2) due to their intrinsically low density of active sites. Perovskites (e.g., $LaCoO_3$) have been reported to be active catalysts for the ORR but with inferior activity (half-wave potential <0.75 V vs reversible hydrogen electrode (RHE)), likely due to their poor electronic conductivity.[13] As a comparison, 3d metal oxides have attracted increasing attention as ORR electrolysis due to to their high activity, high density of active sites, stable structure, and low cost.[19−29] For example, cobalt and manganese monoxides (CoO and MnO) with a rock-salt structure were reported to be active for catalyzing the oxygen reduction.[30−33] However, the reported activities in alkaline media yielded half-wave potentials ($E_{1/2}$) less than 0.8 V vs the reversible hydrogen electrode (RHE), which is much lower than the benchmark activity of Pt/C (0.89 V vs RHE). Previously, we showed that Mn−Co oxides exhibited a promising ORR activity in RDE measurements and achieved a high peak power density of over 1 W/cm^2 in membrane electrode assembly (MEA) measurements.[19,20] In this work, we went one step further to explore Mn−Co bimetallic oxides with different crystal structures to better understand the catalyst structure and the observed ORR activity. We discovered a new compound, $MnCo_2O_3$, with a rock-salt-type structure that exhibited a remarkable ORR activity. The methodology of structural analysis described in this work could help understand the microstructure of other catalysts, at the atomic scale, and build correlations to the catalytic activity.

RESULTS AND DISCUSSION

Co_3O_4/C and $MnCo_2O_4$/C with cubic spinel structures were first synthesized through a facile hydrothermal method. Powder X-ray diffraction (XRD) patterns of Co_3O_4/C exhibited the typical features of cubic spinel oxides with a major (311) peak (PDF# 01-071-1178) (Figure S1a). The domain size of the Co_3O_4 nanoparticles (NPs) was estimated to be 18 nm based on the Scherrer equation. Co_3O_4/C was then partially reduced to CoO/C under mild NH_3 reduction at 300 °C for 3 h (referred to CoO/C-N300). The resulting

Received: July 15, 2019
Revised: October 30, 2019
Published: October 31, 2019

DOI: 10.1021/acs.chemmater.9b02801
Chem. Mater. XXXX, XXX, XXX−XXX

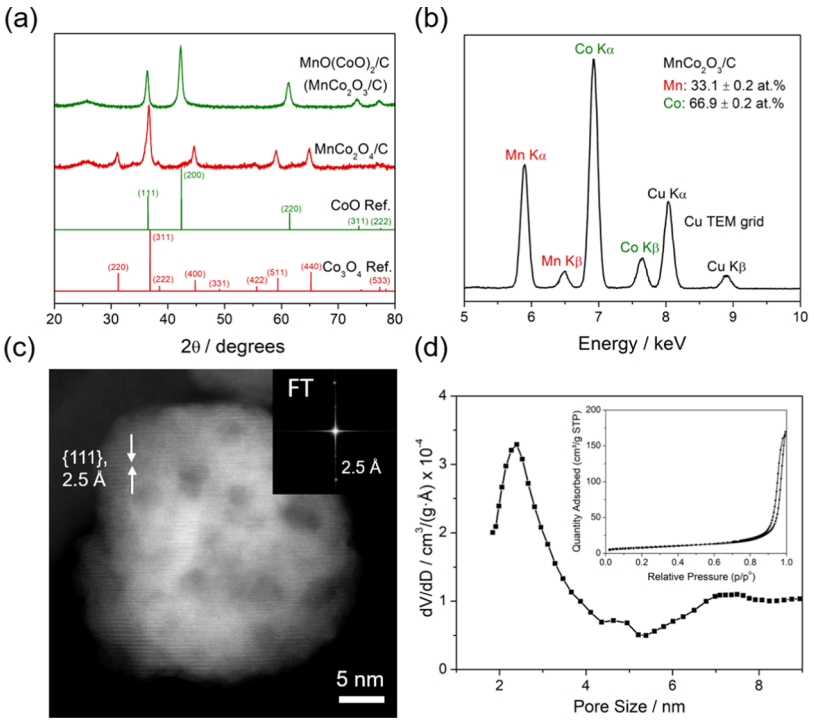

Figure 1. (a) Powder XRD patterns of $MnCo_2O_3$/C, $MnCo_2O_4$/C compared to standard XRD patterns of CoO and Co_3O_4. (b) TEM−EDX spectrum of $MnCo_2O_3$/C showing the relative Co/Mn atomic ratio of 2:1. (c) Atomic-scale STEM image of $MnCo_2O_3$/C with {111} d-spacings and the corresponding Fourier transform (FT). (d) Differential pore volume distribution (dV/dD profile) as a function of pore size of $MnCo_2O_3$ without carbon support and the corresponding N_2 adsorption−desorption BET isotherm (inset).

CoO/C-N300 exhibited a single-phase XRD pattern as the CoO XRD reference (PDF# 01-076-1802) with a slightly smaller domain size of 14 nm. As a fingerprint of the chemical environment of Co, electron energy-loss near-edge structure (ELNES) spectra of CoO/C-N300 exhibited nearly identical features as the CoO reference, indicating that CoO/C-N300 shared the same chemical environment of Co(II) as CoO (Figure S1b). Comparisons in the crystal structure of Co_3O_4 and CoO are demonstrated in Figure S2. During NH_3 treatment, some of the oxygen atoms in the spinel Co_3O_4 were removed to form the rock-salt-type CoO. Consequently, the coordination numbers (CN) of Co changed from the co-existence of tetrahedral [CoO_4] and octahedral [CoO_6] in Co_3O_4 to all octahedral [CoO_6] in CoO (Figure S2).

Following the successful synthesis of CoO/C NPs, $MnCo_2O_4$/C spinel oxides were synthesized and used as precursors for further NH_3 treatment at 300 °C. As shown in Figure 1a, Mn−Co bimetallic oxides exhibited a similar rock-salt-type structure to the CoO reference with a major (200) peak. Thus, we propose that this new compound has a chemical formula of $MnO(CoO)_2$/C or simply $MnCo_2O_3$/C. It has been reported that CoO and MnO could form a miscible solid solution, bulk-phase $Co_xMn_{1-x}O$ ($0 < x < 1$) under high-temperature (1100 °C) sintering.[34] The domain sizes of the nanoparticles were calculated to be 15 nm for $MnCo_2O_4$/C and 13 nm for $MnCo_2O_3$/C. The chemical composition of $MnCo_2O_3$/C was determined by X-ray energy-dispersive spectroscopy (EDX) (Figure 1b), based on the Cliff−Lorimer equation.[35] $MnCo_2O_3$/C exhibited relative contents of 33.1 atom % Mn and 66.9 atom % Co (relative error: 0.2% was defined as one standard deviation), which matched the theoretical values of 33.3 and 66.6% in $MnCo_2O_3$, respectively. Since NH_3 was used as a mild reducing agent, it is important to know whether any N was introduced into the product during the synthesis. As shown in Figure S3, no evidence of a N signal from $MnCo_2O_3$/C was found to be above the detection limit of EDX, electron energy-loss spectroscopy (EELS), and X-ray photoelectron spectroscopy (XPS) characterizations.

The morphology and crystal structure of $MnCo_2O_3$/C were examined using aberration-corrected high-angle annular dark-field scanning transmission electron microscopy (HAADF-STEM) imaging at 100 keV (Nion UltraSTEM). $MnCo_2O_3$/C exhibited a particle size of 30−50 nm embedded in a Ketjen black (KB) carbon matrix (Figure S4), indicating that the majority of particles have multiple subdomains, given an XRD domain size of about 13 nm. Atomic-scale STEM images of individual $MnCo_2O_3$ nanoparticles showed single-crystal features with d-spacings of 2.5 Å, as indicated by the diffraction spots in the Fourier transform, which were the same as the {111} d-spacings of CoO (2.46 Å) within the STEM spatial resolution (Figure 1c). The lattice images of $MnCo_2O_3$ showed a nonuniform image intensity, suggesting the existence of nm scale mesoporous morphology, which was also found in many other $MnCo_2O_3$ NPs (Figure S5). To quantify the porosity of $MnCo_2O_3$ NPs, a N_2 adsorption−desorption test was performed on $MnCo_2O_3$ without KB carbon support since the larger surface area of carbon (900 m^2/g) would likely dominate the measured surface area in the catalyst/carbon composite. The specific surface area of $MnCo_2O_3$ NPs was estimated to be 30 ± 0.1 m^2/g by the Brunauer−Emmett−Teller (BET) method (Figure 1d, inset). The pore size distribution of $MnCo_2O_3$, derived from the Barrett−Joyer−Halenda (BJH) method suggested a narrow size distribution with an average pore size of 2.4 nm (Figure 1d), which was consistent with the pore size in STEM images (Figures 1c and S5). $MnCo_2O_3$/C exhibited a similar pore size

DOI: 10.1021/acs.chemmater.9b02801
Chem. Mater. XXXX, XXX, XXX−XXX

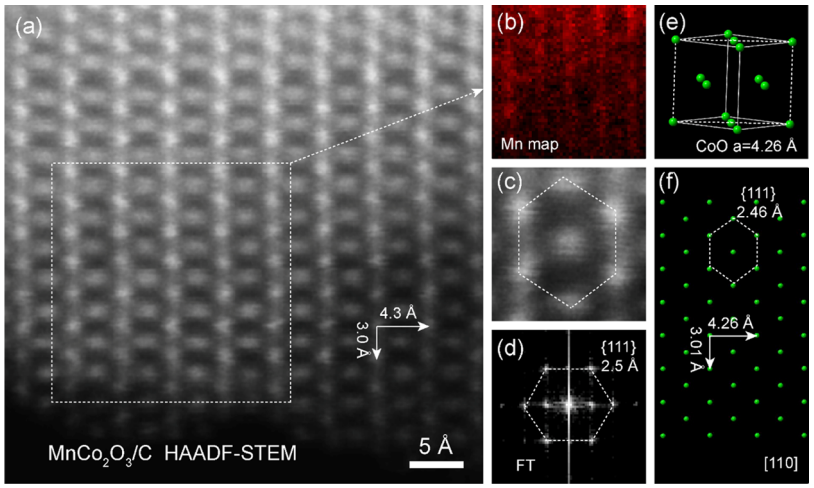

Figure 2. Atomic-scale HAADF-STEM image of rock-salt-type $MnCo_2O_3$/C. (a) Overall lattice image of $MnCo_2O_3$ on the zone axis of [110]. (b) Atomic-scale EELS elemental map of Mn acquired from the dashed box in (a). (c) The magnified single unit cell of $MnCo_2O_3$ showing the typical hexagonal symmetry. (d) Fourier transform (FT) of lattice image in (a) showing the corresponding hexagonal symmetry with {111} d-spacing (2.5 Å). (e) Unit cell of rock-salt-type CoO (lattice parameter, a = 4.26 Å) based on PDF# 01-071-1178. Dashed lines indicate the lattice planes proportional to the [110] zone axis. (f) 2D projection of the crystal model exhibiting the hexagonal symmetry with {111} d-spacings of 2.46 Å. Theoretical lattice spacings of 4.26 and 3.01 Å are consistent with experimental values of 4.3 and 3.0 Å in (a).

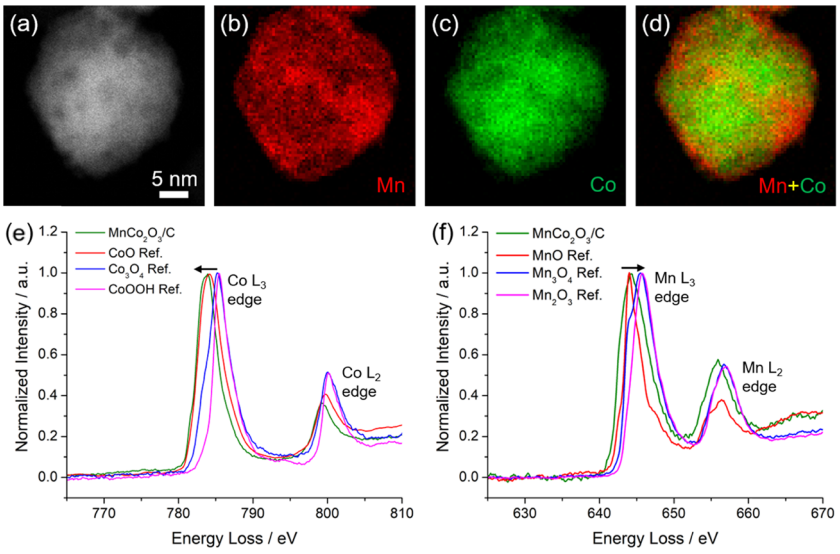

Figure 3. STEM−EELS elemental mapping and fine spectroscopic analysis of $MnCo_2O_3$/C. (a−d) STEM images of one $MnCo_2O_3$ nanoparticle and the corresponding EELS elemental maps of Mn (red), Co (green) and composite map of Mn vs Co. (e) Electron energy-loss near-edge structure (ELNES) of Co $L_{3,2}$ edges of $MnCo_2O_3$/C and reference Co oxides, CoO, Co_3O_4, and CoOOH. (f) ELNES spectra of Mn $L_{3,2}$ edges of $MnCo_2O_3$/C and reference Mn oxides, MnO, Mn_3O_4, Mn_2O_3. Black arrows in (e, f) indicate the negative and positive shifts of Co and Mn L_3 edges, relative to CoO and MnO references, respectively.

distribution as the KB support, which had undergone the same hydrothermal treatment and subsequent annealing in NH_3 gas. It indicates that $MnCo_2O_3$ did not significantly change the porosity of KB (Figure S6). The spinel precursor, $MnCo_2O_4$, was found to have a similar BET surface area of 34.1 ± 0.3 m^2/g, indicating no significant changes in the surface area during NH_3 treatment (Figure S7).

The crystal structure of $MnCo_2O_3$ was then directly visualized using atomic-scale STEM imaging and EELS mapping. As shown in Figure 2a, $MnCo_2O_3$ exhibited atom columns with two perpendicular d-spacings of 4.3 and 3.0 Å on the [110] zone axis, which were consistent with the theoretical values of 4.26 and 3.01 Å, based on the crystal model of CoO (Figure 2f). The [110] zone axis is proportional to the lattice plane indicated by the dashed rectangles in the unit cell of CoO (Figure 2e). The d-spacings of 3.01 Å can be obtained by dividing the lattice parameter, 4.26 Å by $\sqrt{2}$ due to a projection angle of 45°. The magnified image in Figure 2c showed the characteristic hexagonal symmetry on the [110] zone axis of CoO. The corresponding Fourier transform (FT) in Figure 2d displayed the hexagonal arrangements of diffraction spots with {111} d-spacings of 2.5 Å, which matched well the theoretical values of 2.46 Å in the crystal model in Figure 2f. Besides the imaging analysis on crystal structures, atomic-scale EELS mapping was employed to extract chemical composition using metal L_3 edges (Figure S8). An atomic-scale EELS map of Mn exhibited a clear

DOI: 10.1021/acs.chemmater.9b02801
Chem. Mater. XXXX, XXX, XXX−XXX

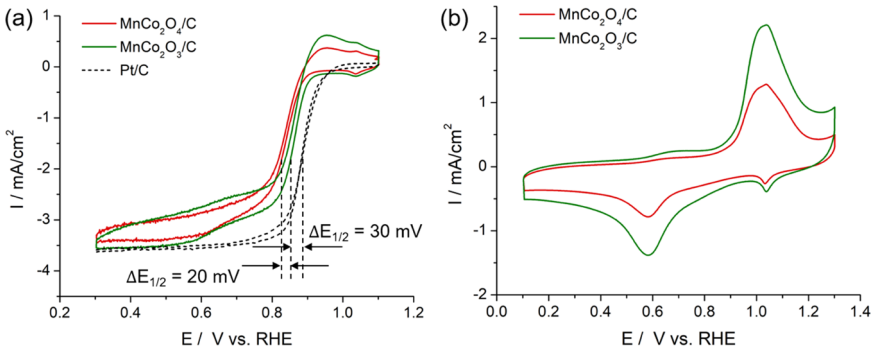

Figure 4. (a) ORR polarization profiles of $MnCo_2O_4$/C, $MnCo_2O_3$/C, and Pt/C in O_2-sat. 1 M KOH at 1600 rpm and 5 mV/s. Metal oxides and Pt mass loadings are 0.1 mg/cm^2 and 25 μg/cm^2, respectively. (b) CV profiles of $MnCo_2O_4$/C and $MnCo_2O_3$/C in Ar-sat. 1 M KOH at 10 mV/s.

layered structure, indicating the successful incorporation of Mn into the Co-based rock-salt-type structures at the atomic scale.

The chemical composition was investigated using electron energy-loss spectroscopy (EELS). Figure 3a–c presents the STEM image of one $MnCo_2O_3$ nanoparticle and the corresponding EELS elemental maps of Mn in red and Co in green. The composite map of Mn vs Co in Figure 3d suggests a Co-rich core with a thin Mn-rich shell of 1–3 nm, which was further evidenced by EELS maps of other $MnCo_2O_3$ NPs (Figure S9). The electron energy-loss near-edge structure (ELNES) analysis offers microstructural analysis with atomic-scale spatial resolution and high-energy resolution (0.5 eV) simultaneously. ELNES serves as a "fingerprint" to probe the local electronic structure, i.e., density of unfilled states (unfilled density of states (DOS)) above the Fermi level (E_F), which is particularly sensitive to the local atomic environment, such as valence state, chemical bonding, and coordination environment.[36] ELNES spectra of Co and Mn L edges were aligned against the zero loss peak (ZLP) and found to have high reproducibility among five different regions on the TEM grids (Figure S10a,b). Given the existence of a thin Mn shell in $MnCo_2O_3$/C, ELNES spectra of Co and Mn in core and shell sections were extracted separately from spectrum images to identify any inhomogeneities of electronic structures between the core and shell. As shown in Figure S10c,d, Co and Mn in core and shell sections shared nearly the same features in ELNES spectra, indicating a homogeneous local valence distribution despite the heterogenous elemental distribution with a Mn-rich shell.

To further identify the valence state of active sites of the electrocatalysts, ELNES spectra of $MnCo_2O_3$/C were compared to Co and Mn reference oxides (Figure 3e,f). Co and Mn L_3 edges of $MnCo_2O_3$/C exhibited similar features to CoO and MnO references (green and red lines in Figure 3e,f) and were distinct from the ELNES spectra of Co_3O_4(II,III), Mn_3O_4(II,III), CoOOH(III), and Mn_2O_3(III). It has been suggested that Co and Mn in $MnCo_2O_3$/C share the same rock-salt-type structures as CoO(II) and MnO(II), respectively. Furthermore, Co L_3 edge showed a slightly negative shift, relative to CoO(II), while the Mn L_3 edge had a slightly positive shift, relative to MnO(II). This symmetrical spectra shift indicated a local charge transfer from Mn to Co and a possible synergistic effect between the two of them, serving as co-active sites, which is consistent with our observation on Co–Mn spinel oxides using in situ X-ray absorption spectroscopy (XAS).[28,29] Besides the relative peak position, the intensity ratio of L_2/L_3 edges also reveals the covalency of metal–oxygen bonds.[37] A higher L_2/L_3 ratio indicates a more covalent bond, as shown by the difference between CoO(II) and CoOOH(III) and between MnO(II) and Mn_2O_3(III) (Figure 3e,f). Co in $MnCo_2O_3$/C exhibited an even lower L_2/L_3 ratio than CoO(II), while Mn in $MnCo_2O_3$/C showed a much higher L_2/L_3 ratio than MnO (II), suggesting a less covalent (more ionic) Co–O bond and symmetrically a more covalent Mn–O, relative to CoO and MnO, respectively. Apart from the metal L edges, oxygen K-edge can also provide a complementary picture of the metal–oxygen binding environment. The first and second peaks in ELNES spectra of the O K-edge represent the O 2p character in metal partially filled 3d bands and empty 4s,p bands, respectively (Figure S11). The O K-edge of $MnCo_2O_3$/C resembled the features of CoO and MnO rather than other reference oxides with higher valence (Figure S11a,b). More specifically, the O K-edge of $MnCo_2O_3$/C is more similar to CoO than MnO since Co is the majority metal in $MnCo_2O_3$/C (Figure S11a).

After thorough structural investigation, the well-defined rock-salt-type $MnCo_2O_3$/C as well as the spinel-type $MnCo_2O_4$/C materials were employed as oxygen reduction electrocatalysts in alkaline fuel cells. ORR polarization profiles were acquired in O_2-saturated 1 M KOH at 1600 rpm and 5 mV/s using a rotating disk electrode (Pine Instruments). $MnCo_2O_3$/C with a loading of 0.1 mg/cm^2 exhibited a promising ORR activity with a half-wave potential ($E_{1/2}$ = 0.86 V vs a reversible hydrogen electrode, RHE). This is 20 mV higher than that of the spinel $MnCo_2O_4$/C ($E_{1/2}$ = 0.84 V), corresponding to about 2-fold enhancement in mass-specific activity (Figure 4a). The $E_{1/2}$ of $MnCo_2O_3$/C is only 30 mV away from the benchmark 20 wt % Pt/C ($E_{1/2}$ = 0.89 V), making $MnCo_2O_3$/C a promising nonprecious ORR electrocatalyst for alkaline fuel cells. It should be noted that the catalytic activities were preliminarily evaluated employing RDE measurements, while the more realistic MEA measurements are currently under investigation. $MnCo_2O_3$/C is able to reach the same diffusion-limited current density (−3.6 mA/cm^2), I_d, as Pt/C, suggesting a 4e$^-$ process of reducing O_2 completely to H_2O. It is important to note that, based on the Levich equation, the I_d of the 4e$^-$ reduction of oxygen in 0.1 M oxygen-saturated KOH or $HClO_4$ should be −5.5 mA/cm^2 at 1600 rpm. Since the O_2 solubility (CO_2) in 1 M KOH at 25 °C and 1 atm is 8.42×10^{-4} mol/L, which is 70% of the CO_2 in 0.1 M KOH (1.21×10^{-3} mol/L),[38] the I_d of the 4e$^-$ ORR in 1 M KOH will be correspondingly lower with a value of about −3.8 mA/cm^2 at 1600 rpm. Additionally, as shown in Figure S13, $MnCo_2O_3$/C and $MnCo_2O_4$/C have smaller Tafel slopes

DOI: 10.1021/acs.chemmater.9b02801
Chem. Mater. XXXX, XXX, XXX–XXX

of 45 and 50 mV/dec, respectively, relative to Pt/C (60 mV/dec), suggesting a smaller overpotential to achieve the same kinetic current change. To investigate the catalyst surface, cyclic voltammetric (CV) profiles of $MnCo_2O_3$/C and $MnCo_2O_4$/C were acquired, which showed that $MnCo_2O_3$/C had a larger redox current than $MnCo_2O_4$/C, indicating the existence of more active sites in $MnCo_2O_3$/C (Figure 4b). Both $MnCo_2O_4$/C and $MnCo_2O_3$/C shared a similar redox peak position, indicating a similar catalyst surface, which actually matched our previous observation that spine-type $MnCo_2O_4$/C has a shell rich in CoO(II) and a core rich in Co_3O_4 (Figure S12). The small reduction peak at 1.1 V vs RHE was separated from the main peak by changing the lower scan limit of the CV profile (Figure S14). It was identified as monolayer species on the Mn-rich shell with a highly reversible redox process.

In an attempt to implement a Pt-free cathode for AEMFCs, nonprecious ORR electrocatalysts are required to not only satisfy the initial activity requirements but also survive long-term durability tests.[2] Catalyst durability was examined by following an accelerated aging protocol: continuous 10 000 CV cycles at 10 mV/s from 0.6 to 1.0 V vs RHE in O_2-sat. 1 M KOH (Figure S15a). $MnCo_2O_3$/C exhibited a mild decay in ORR activity after 10K cycles as the $E_{1/2}$ shifted from 0.86 to 0.84 V. The activity decay of $MnCo_2O_3$/C is comparable to or slightly better than Pt/C ($\Delta E_{1/2}$ = 25 mV after 10K cycles) under same test conditions (Figure S16). The activity decay of Pt/C was mainly ascribed to the loss of electrochemical surface area (ECSA), as shown in the CV profiles of Pt/C. Noticeably, the activity of $MnCo_2O_3$/C after 10K cycles was still comparable to the initial activity of $MnCo_2O_4$/C. A noticeable loss in the I_d was found in both $MnCo_2O_3$/C and $MnCo_2O_4$/C, suggesting a loss of surface area, possibly due to particle aggregation during cycles. Further strategies to enhance the catalyst−support interactions will be critical to mitigate the particle aggregation and extend the lifetime of nonprecious metal oxide electrocatalysts. TEM−EDX spectra were used to quantitatively investigate the changes in chemical composition after durability tests. Mn and Co Kα edges were used to quantify the relative contents of Mn and Co (Figure S15b). They showed that the Mn content increased slightly from 33.1 ± 0.2 to 35.9 ± 0.4 atom % (Table S1).

CONCLUSIONS

In summary, a new rock-salt-type Mn−Co oxide $MnCo_2O_3$/C was discovered by treating $MnCo_2O_4$/C in a mild reducing agent, NH_3. The microstructure and chemical environment were comprehensively investigated by atomic-scale STEM imaging, EDX, EELS, and ELNES spectroscopic analysis. The promising ORR activity of $MnCo_2O_3$/C is likely due to rationally designed nanostructure with Mn and Co serving as synergistically active sites. This in-depth structural investigation will offer insightful strategies for material design and developments in the renewable energy community, in general, and in fuel cells, in particular.

EXPERIMENTAL SECTION

Material Synthesis. $Mn(Ac)_2{\cdot}4H_2O$ and $Co(Ac)_2{\cdot}4H_2O$ were dissolved in 15 mL of deionized (DI) water and sonicated for 15 min. Concentrated $NH_3{\cdot}H_2O$ (500 μL) was diluted in 5 mL of DI water and added to the metal precursor solution dropwise under vigorous stirring at 1200 rpm. The pH of the formed metal−NH_3 complex solution was tested and controlled to be around 11. Ethanol (20 mL) was later added to the metal−NH_3 complex solution with an EtOH/H_2O volume ratio of 1:1. Ketjen Black (KB) with a BET surface area of 900 m^2/g was added to the resulting suspension/solution, which was kept stirring at 1200 rpm and 60 °C for 12 h. The solution was then transferred into a 50 mL autoclave for the hydrothermal reaction at 150 °C for 3 h. Co_3O_4 and $MnCo_2O_4$ supported on carbon (40 wt %) were separated from the residual solution using a centrifuge at 6000 rpm and washed with EtOH/H_2O (vol 1:1) three times and oven-dried at 80 °C for 6h. Rock-salt-type CoO/C and $MnCo_2O_3$/C were formed by treating the as-synthesized Co_3O_4/C and $MnCo_2O_4$/C in NH_3 at 300 °C for 3 h with a temperature ramping rate of 5 °C/min. NH_3 treatment at higher temperatures would introduce metallic or metal nitride impurity phases, and H_2 treatment at 300 °C would lead to the formation of metallic Co. $MnCo_2O_3$ NPs with no carbon support were prepared from $MnCo_2O_4$ NPs with no carbon support, which was synthesized using the same hydrothermal procedures except without adding carbon during the synthesis.

Structural Characterization. The crystal structures of all of the synthesized electrocatalysts were examined by powder X-ray diffraction (XRD) using a Rigaku Ultima IV Diffractometer. Diffraction patterns were collected at a scan rate of 2 °/min at 0.02° steps from 20 to 80°. Specific surface area and pore size distributions were analyzed based on Brunauer−Emmett-Teller (BET) and Barrett−Joyner−Halenda (BJH) methods from the N_2 adsorption−desorption isotherms acquired at −195 °C (liquid N_2) in a Micromeritics ASAP2020 instrument. XPS spectra were acquired using a Surface Science Instruments SSX-100 with an operating pressure of 2×10^{-9} Torr. Monochromatic Al Kα X-rays (1486.6 eV) with 1 mm diameter beam size were used. Photoelectrons were collected at a 55° emission angle. A hemispherical analyzer determined electron kinetic energy using a pass energy of 150 V for wide/survey scans and 50 V for high-resolution scans. Scanning transmission electron microscopy (STEM) images and elemental electron energy-loss spectroscopy (EELS) maps were acquired on a fifth-order aberration-corrected STEM (Cornell Nion UltraSTEM) operated at 100 keV with a beam convergence semiangle of 30 mrad. TEM−EDX spectra were collected in a FEI Tecnai F-20 electron microscope equipped with an Oxford X-Max detector. Detailed S/TEM analysis can be found in the Supporting Information.

Electrochemical Characterization. Electrocatalysts (5.0 mg) were mixed with 1.0 mL of 0.05 wt % Nafion/ethanol solution and, subsequently, sonicated for approximately 30 min to form a homogeneous catalyst ink. The resulting catalyst ink (10 μL) was loaded onto a glassy carbon (GC) electrode (D = 5.0 mm, Pine Instruments) as the working electrode (WE), achieving a metal oxide loading of 0.1 mg/cm^2, followed by thermal evaporation of the solvent under infrared light. Similarly, 5 μL of a Pt/C catalyst ink was loaded onto a GC electrode to achieve a loading of 25 $\mu g/cm^2$, a common value for comparison in fuel cell tests. Ag/AgCl in the saturated KCl solution was served as the reference electrode (RE), and a large area graphite rod was used as the counter electrode (CE). More experimental details can be found in the Supporting Information.

ASSOCIATED CONTENT

Supporting Information

The Supporting Information is available free of charge on the ACS Publications website at DOI: 10.1021/acs.chemmater.9b02801.

Electron microscopy characterization; electrochemical characterization; powder XRD patterns; crystal structures; EDX, EELS, XPS spectra; STEM images; pore size distribution (Figures S1−S16 and Table S1) (PDF)

AUTHOR INFORMATION

Corresponding Author

*E-mail: hda1@cornell.edu.

DOI: 10.1021/acs.chemmater.9b02801
Chem. Mater. XXXX, XXX, XXX−XXX

ORCID

Yao Yang: 0000-0003-0321-3792
Rui Zeng: 0000-0002-7577-767X
Héctor D. Abruña: 0000-0002-3948-356X

Notes

The authors declare no competing financial interest.

■ ACKNOWLEDGMENTS

This work was primarily supported by the Center for Alkaline-Based Energy Solutions (CABES), part of the Energy Frontier Research Center (EFRC) program supported by the U.S. Department of Energy, under grant DE-SC-0019445. This work made use of TEM facilities at the Cornell Center for Materials Research (CCMR), which are supported through the National Science Foundation Materials Research Science and Engineering Center (NSF MRSEC) program (DMR-1719875). We are grateful to Malcolm (Mick) Thomas at CCMR for the help in Nion UltraSTEM. We appreciate the help in BET tests from Mary Zick in the Milner group at Cornell University.

■ REFERENCES

(1) Debe, M. K. Electrocatalyst Approaches and Challenges for Automotive Fuel Cells. *Nature.* **2012**, *486*, 43−51.
(2) Gasteiger, H. A.; Kocha, S. S.; Somali, B.; Wagner, F. T. Activity Benchmarks and Requirements for Pt, Pt-alloy, and non-Pt Oxygen Reduction Catalysts for PEMFCs. *Appl. Catal., B.* **2005**, *56*, 9−35.
(3) Xiong, Y.; Yang, Y.; Joress, H.; Padgett, E.; Gupta, U.; Yarlagadda, V.; Agyeman-Budu, D. N.; Huang, X.; Moylan, T. E.; Zeng, R.; Kongkanand, A.; Escobedo, F. A.; Brock, J. D.; DiSalvo, F. J.; Muller, D. A.; Abruña, H. D. Revealing the Atomic Ordering of Binary Intermetallics Using in Situ Heating Techniques at Multilength Scales. *Proc. Natl. Acad. Sci. U.S.A.* **2019**, *116*, 1974−1983.
(4) Papageorgopoulos, D. *2017 Annual Merit Review and Peer Evaluation Meeting in Fuel Cells Program Area*, U.S. Department of Energy: Washington, DC, 2017.
(5) Wang, D.; Xin, H. L.; Hovden, R.; Wang, H.; Yu, Y.; Muller, D. A.; DiSalvo, F. J.; Abruña, H. D. Structurally Ordered Intermetallic Platinum-Cobalt Core-Shell Nanoparticles with Enhanced Activity and Stability as Oxygen Reduction Electrocatalysts. *Nat. Mater.* **2013**, *12*, 81−87.
(6) Xiong, Y.; Yang, Y.; DiSalvo, F. J.; Abruña, H. D. Pt-Decorated Composition-Tunable Pd−Fe@Pd/C Core−Shell Nanoparticles with Enhanced Electrocatalytic Activity toward the Oxygen Reduction Reaction. *J. Am. Chem. Soc.* **2018**, *140*, 7248−7255.
(7) Xiong, Y.; Xiao, L.; Yang, Y.; DiSalvo, F. J.; Abruña, H. D. High-Loading Intermetallic Pt_3Co/C Core−Shell Nanoparticles as Enhanced Activity Electrocatalysts toward the Oxygen Reduction Reaction (ORR). *Chem. Mater.* **2018**, *30*, 1532−1539.
(8) Wang, G.; Huang, B.; Xiao, L.; Ren, Z.; Chen, H.; Wang, D.; Abruña, H. D.; Lu, J.; Zhuang, L. Pt Skin on AuCu Intermetallic Substrate: A Strategy to Maximize Pt Utilization for Fuel Cells. *J. Am. Chem. Soc.* **2014**, *136*, 9643−9649.
(9) Lu, S.; Pan, J.; Huang, A.; Zhuang, L.; Lu, J. Alkaline Polymer Electrolyte Fuel Cells Completely Free from Noble Metal Catalysts. *Proc. Natl. Acad. Sci. U.S.A.* **2008**, *105*, 20611−20614.
(10) Pan, J.; Chen, C.; Zhuang, L.; Lu, J. Designing Advanced Alkaline Polymer Electrolytes for Fuel Cell Applications. *Acc. Chem. Res.* **2012**, *45*, 473−481.
(11) Chung, H. T.; Cullen, D. A.; Higgins, D.; Sneed, B. T.; Holby, E. F.; More, K. L.; Zelenay, P. Direct Atomic-Level Insight into the Active Sites of a High-Performance PGM-Free ORR Catalyst. *Science* **2017**, *357*, 479−484.
(12) Ren, H.; Wang, Y.; Yang, Y.; Tang, X.; Peng, Y.; Peng, H.; Xiao, L.; Lu, J.; Abruña, H. D.; Zhuang, L. Fe/N/C Nanotubes with Atomic Fe Sites: A Highly Active Cathode Catalyst for Alkaline Polymer Electrolyte Fuel Cells. *ACS Catal.* **2017**, *7*, 6485−6492.
(13) Suntivich, J.; Gasteiger, H. A.; Yabuuchi, N.; Nakanishi, H.; Goodenough, J.; Shao-Horn, Y. Design Principles for Oxygen-Reduction Activity on Perovskite Oxide Catalysts for Fuel Cells and Metal−Air Batteries. *Nat. Chem.* **2011**, *3*, 647.
(14) Xiong, Y.; Yang, Y.; DiSalvo, F. J.; Abruña, H. D. Metal-Organic-Framework-Derived Co-Fe Bimetallic Oxygen Reduction Electrocatalyst for Alkaline Fuel Cells. *J. Am. Chem. Soc.* **2019**, *141*, 10744−10750.
(15) Huang, K.; Liu, J.; Wang, L.; Chang, G.; Wang, R.; Lei, M.; Wang, Y.; He, Y. Mixed Valence $CoCuMnO_x$ Spinel Nanoparticles by Sacrificial Template Method with Enhanced ORR Performance. *Appl. Surf. Sci.* **2019**, *487*, 1145−1151.
(16) He, X.; Luan, S. Z.; Wang, L.; Wang, R. Y.; Du, P.; Xu, Y. Y.; Yang, H. J.; Wang, Y. G.; Huang, K.; Lei, M. Facile Loading Mesoporous Co_3O_4 on Nitrogen Doped Carbon Matrix as an Enhanced Oxygen Electrode Catalyst. *Mater. Lett.* **2019**, *244*, 78−82.
(17) Negro, E.; Nale, A.; Vezzù, K.; Pagot, G.; Herve Bang, Y.; Polizzi, S.; Colombo, M.; Prato, M.; Crociani, L.; Bonaccorso, F.; Noto, V. D. $(Co,Ni)Sn_{0.5}$ Nanoparticles Supported on Hierarchical Carbon Nitride-Graphene-Based Electrocatalysts for the Oxygen Reduction Reaction. *ChemElectroChem* **2018**, *5*, 2029−2040.
(18) Negro, E.; Bach Delpeuch, A.; Vezzù, K.; Nawn, G.; Bertasi, F.; Ansaldo, A.; Pellegrini, V.; Dembinska, B.; Zoladek, S.; Miecznikowski, K.; Rutkowska, I. A.; Skunik-Nuckowska, M.; Kulesza, P. J.; Bonaccorso, F.; Noto, V. D. Toward Pt-Free Anion-Exchange Membrane Fuel Cells: Fe-Sn Carbon Nitride-Graphene Core-Shell Electrocatalysts for the Oxygen Reduction Reaction. *Chem. Mater.* **2018**, *30*, 2651−2659.
(19) Wang, Y.; Yang, Y.; Jia, S.; Wang, X.; Lyu, K.; Peng, Y.; Zheng, H.; Wei, X.; Ren, H.; Xiao, L.; Wang, J.; Muller, D. A.; Abruña, H. D.; Hwang, B. J.; Lu, J.; Zhuang, L. Synergistic Mn-Co Catalyst Outperforms Pt on High-Rate Oxygen Reduction Reaction for Alkaline Polymer Electrolyte Fuel Cells. *Nat. Commun.* **2019**, *10*, No. 1506.
(20) Yang, Y.; Peng, H.; Xiong, Y.; Li, Q.; Lu, J.; Xiao, L.; DiSalvo, F.; Zhuang, L.; Abruña, H. High-Loading Composition-Tolerant Co-Mn Spinel Oxides with Performance beyond 1 W/cm^2 in Alkaline Polymer Electrolyte Fuel Cells. *ACS Energy Lett.* **2019**, *4*, 1251−1257.
(21) Peng, X.; Omasta, T. J.; Magliocca, E.; Wang, L.; Varcoe, J. R.; Mustain, W. E. N-doped Carbon CoO_x Nanohybrids: The First Precious Metal Free Cathode to Achieve 1.0 W/cm^2 Peak Power and 100 h Life in Anion-Exchange Membrane Fuel Cells. *Angew. Chem., Int. Ed.* **2019**, *58*, 1046−1051.
(22) Liang, Y.; Li, Y.; Wang, H.; Zhou, J.; Wang, J.; Regier, T.; Dai, H. Co_3O_4 Nanocrystals on Graphene as a Synergistic Catalyst for Oxygen Reduction Reaction. *Nat. Mater.* **2011**, *10*, 780−786.
(23) Meng, Y.; Song, W.; Huang, H.; Ren, Z.; Chen, S.; Suib, S. Structure−Property Relationship of Bifunctional MnO_2 Nanostructures: Highly Efficient, Ultra-Stable Electrochemical Water Oxidation and Oxygen Reduction Reaction Catalysts Identified in Alkaline Media. *J. Am. Chem. Soc.* **2014**, *136*, 11452−11464.
(24) Liang, Y.; Wang, H.; Zhou, J.; Li, Y.; Wang, J.; Regier, T.; Dai, H. Covalent Hybrid of Spinel Manganese−Cobalt Oxide and Graphene as Advanced Oxygen Reduction Electrocatalysts. *J. Am. Chem. Soc.* **2012**, *134*, 3517−3523.
(25) Li, C.; Han, X.; Cheng, F.; Hu, Y.; Chen, C.; Chen, J. Phase and Composition Controllable Synthesis of Cobalt Manganese Spinel Nanoparticles towards Efficient Oxygen Electrocatalysis. *Nat. Commun.* **2015**, *6*, No. 7345.
(26) Wei, C.; Feng, Z.; Scherer, G.; Barber, J.; Shao-Horn, Y.; Xu, Z. Cations in Octahedral Sites: A Descriptor for Oxygen Electrocatalysis on Transition-Metal Spinels. *Adv. Mater.* **2017**, *29*, No. 1606800.
(27) Indra, A.; Menezes, P.; Sahraie, N.; Bergmann, A.; Das, C.; Tallarida, M.; Schmeißer, D.; Strasser, P.; Driess, M. Unification of Catalytic Water Oxidation and Oxygen Reduction Reactions: Amorphous Beat Crystalline Cobalt Iron Oxides. *J. Am. Chem. Soc.* **2014**, *136*, 17530−17536.

DOI: 10.1021/acs.chemmater.9b02801
Chem. Mater. XXXX, XXX, XXX−XXX

(28) Yang, Y.; Wang, Y.; Xiong, Y.; Huang, X.; Shen, L.; Huang, R.; Wang, H.; Pastore, J. P.; Yu, S.-H.; Xiao, L.; Brock, J. D.; Zhuang, L.; Abruña, H. D. In Situ X-ray Absorption Spectroscopy of a Synergistic Co−Mn Oxide Catalyst for the Oxygen Reduction Reaction. *J. Am. Chem. Soc.* **2019**, *141*, 1463−1466.
(29) Xiong, Y.; Yang, Y.; Feng, X.; DiSalvo, F. J.; Abruña, H. D. A Strategy for Increasing the Efficiency of the Oxygen Reduction Reaction in Mn-Doped Cobalt Ferrites. *J. Am. Chem. Soc.* **2019**, *141*, 4412−4421.
(30) Liu, J.; Jiang, L.; Zhang, B.; Jin, J.; Su, D. S.; Wang, S.; Sun, G. Controllable Synthesis of Cobalt Monoxide Nanoparticles and the Size-Dependent Activity for Oxygen Reduction Reaction. *ACS Catal.* **2014**, *4*, 2998−3001.
(31) Guo, S.; Zheng, S.; Wu, L.; Sun, S. Co/CoO Nanoparticles Assembled on Graphene for Electrochemical Reduction of Oxygen. *Angew. Chem., Int. Ed.* **2012**, *51*, 11770−11773.
(32) Shanmugam, S.; Gedanken, A. MnO Octahedral Nanocrystals and MnO@C Core-Shell Composites: Synthesis, Characterization, and Electrocatalytic Properties. *J. Phys. Chem. B* **2006**, *110*, 24486−24491.
(33) Chen, R.; Yan, J.; Liu, Y.; Li, J. Three-Dimensional Nitrogen-Doped Graphene/MnO Nanoparticle Hybrids as a High-Performance Catalyst for Oxygen Reduction Reaction. *J. Phys. Chem. C* **2015**, *119*, 8032−8037.
(34) Seetharaman, S.; Abraham, K. P. Activity Measurements in CoO-MnO Solid Solutions. *Scr. Metall.* **1969**, *3*, 911−916.
(35) Cliff, G.; Lorimer, G. W. The Quantitative Analysis of Thin Specimens. *J. Microsc.* **1975**, *103*, 203−207.
(36) Williams, D. B.; Carter, C. B. *Transmission Electron Microscopy: A Textbook for Materials Science*, 2nd ed.; Springer: New York, 2009; p 741.
(37) Garvie, L. A. J.; Craven, A. J. High-resolution Parallel Electron Energy-loss Spectroscopy of Mn $L_{2,3}$-Edges in Inorganic Manganese Compounds. *Phys. Chem. Miner.* **1994**, *21*, 191−206.
(38) Davis, R. E.; Horvath, G. L.; Tobias, C. W. The Solubility and Diffusion Coefficient of Oxygen in Potassium Hydroxide Solutions. *Electrochim. Acta* **1967**, *12*, 287−297.

DOI: 10.1021/acs.chemmater.9b02801
Chem. Mater. XXXX, XXX, XXX−XXX